Submitted to the IEEE Journal of Photovoltaics, JPV-2025-03-0101-R. R2

Artificial Soiling Replication of Field Losses on Commercial Photovoltaic Modules

Fang Li, David C. Miller, Sai Tatapudi, and Govindasamy TamizhMani

***Abstract*—This study demonstrates the capabilities of an indoor artificial soiling approach developed to closely replicate the natural, cyclic soil accumulation processes in the field—dust suspension, deposition, and sedimentation/cementation—for a subtropical climate. In this work, a near-field environment is replicated in an artificial soiling cubic chamber through controlled regulation of humidity, temperature, dust type, and dust concentration, based on site-specific historical climate data. Two different models (MA and MB) of full-size commercial photovoltaic modules from a single manufacturer, installed side by side in the mid-Atlantic United States, were retrieved and subjected to artificial soiling experiments and various characterization measurements, including short-circuit current, colorimetry, reflectance, X-ray fluorescence, laser diffraction, and optical microscopy. Both in the field and in our improved field-representative artificial soiling tests, the MA model experienced roughly twice the soiling loss as the MB model. To closely replicate the field soiling losses for a site-specific climate, it is critical to include: (1) the use of field-collected dust with identical dust chemistry and particle distribution instead of standardized ISO 12103 Arizona Road dusts, (2) the use of only a small amount of field-collected dust inside the chamber during the deposition process (e.g., 0.15 g), and (3) the preconditioning of the surface coating for the partial/full dose of UV stress as experienced in the field during sunlight exposure and the abrasion as experienced in the field during regular module cleaning activities, if/as needed. The field-representative artificial soiling method developed here could potentially be adopted for rank ordering of various antisoiling coatings developed by researchers and industry stakeholders.**

***Index Terms*— Artificial soiling, contamination composition, dust concentration, field dust, particle size distribution (PSD), soiling chamber, soiling level ratio.**

I. INTRODUCTION

Solar photovoltaic (PV) system yield can be reduced by the gradual accumulation of dirt, dust, and other organic particles on the glass surface of modules. Soiling is estimated to cause a worldwide annual economic loss of 4–7 billion euros (4.4–7.7 billion U.S. dollars) from higher operating, cleaning, and/or capital expenditures [1], [2]. Soiling loss is dictated by three sets of factors: climatic/environmental, installation, and PV module design, e.g., the surface properties of the cover glass. Climatic and environmental factors depend on the geographical location and season, and they primarily include dust concentration, dust chemistry and particle size distribution, relative humidity, ambient temperature, rain level and frequency, wind speed, and wind direction. Installation factors include tilt angle, orientation with respect to wind direction, tracking/racking configuration, array size, and layout. Factors related to the surface properties of the module's glass include surface texture, surface composition, and surface energy (hydrophobic, hydrophilic, or hybrid), which can vary from one module type/model to another and can also change over time due to natural aging. Individual factors can have either a positive or negative effect on the soil accumulation rate [1], [3].

The overall impact of these factors on soiling loss rate is summarized in TABLE I. Module installations with higher tilt angles will have lower soiling losses [4], [5], and with tracking, they may have even lower soiling losses [6]. Soiling effects can vary both geographically and environmentally. Even within a single site, spatial nonuniformity of soiling can occur due to differences in dew point temperatures. This effect has been observed to cause a 3% difference in power generation [7]. Furthermore, modules mounted on the upper rack in an array exhibited different soiling than those on bottom rack, because the lower modules received rain runoff from the modules on the upper racks [8].

If field environmental and tilt angle conditions are replicated in an artificial soiling testing chamber along with a clear understanding of sequential soiling dynamics/mechanisms, the extent of soiling loss dependence on the surface coating properties can ideally be emulated. Furthermore, the interactions among these factors can be deconvoluted and assessed in a controlled setting. This streamlined artificial soiling approach should allow researchers to determine the relative effectiveness (rank ordering) of surface properties/ coatings on soiling loss in a shorter testing time than the longer evaluations typically conducted under uncontrolled field conditions. Only a limited number of research groups have attempted to design, develop, and demonstrate the usefulness of artificial soiling chambers for the evaluation of coated glass coupons and minimodules. They have experimentally examined soiling impact, focusing on dust chemistry [9], [10], [11], extent of dust accumulation [12], [13], relative humidity (RH) level and sample temperature [14], water cleaning [15],

This work was supported in part by the U.S. Department of Energy under Contract No. DE-AC36-08GO28308 under agreement 38263. *(Corresponding author: Fang Li).*

Fang Li, Sai Tatapudi, and GovindaSamy TamizhMani are with the Photovoltaic Reliability Laboratory at Arizona State University (ASU PRL), Mesa, AZ, 85212, USA (emails: fangli3@asu.edu, statapud@asu.edu, and manit@asu.edu, respectively).

David C. Miller is with the National Renewable Energy Laboratory, Golden, CO, 80401, USA (email: David.Miller@nrel.gov).

Color versions of all figures in this article are available online at http://ieeexplore.ieee.org.

TABLE I. SOILING LOSS RATE DEPENDENCE ON CLIMATIC AND TILT CONDITIONS FOR REPRESENTATIVE SITES. THE CLIMATIC CONDITIONS ARE DEFINED BASED ON THE KÖPPEN-GEIGER CLIMATE CLASSIFICATION [16]. SOILING LOSS RATES FOR OTHER LOCATIONS WORLDWIDE ARE DESCRIBED IN [2]. SOILING LOSS RATE IN %/DAY DENOTES THE AVERAGE SOILING LOSS RATE FITTED LINEARLY USING MODULE PERFORMANCE DATA COLLECTED OVER MONTHS DURING A DRY PERIOD.

Field Location	Climatic Condition	Tilt Angle	Soiling Loss Rate During Dry Field Exposure (%/day)	Reference
California, U.S.	Temperate semi-arid (Steppe)	Tilt angle <5° Tilt angle >20°	>0.1 <0.05	[17]
Southwest U.S.	Arid (Steppe)	1-axis tracker	0.3	[18]
Mumbai, India	Tropical monsoon (Am)	Latitude tilt Vertical tilt	0.43 0.02	[19] [20]
Lahore, Pakistan	Humid subtropical (BSh)	Tilt angle ~30°	0.8	[21]
Arica, Chile	Cold desert (BWk)	Latitude tilt	0.9	[22]
Abu Dhabi, UAE	Hot desert (BWh)	Tilt angle 25°	0.87	[23]

wind effect [24], incident angle effect [25], and coating materials applied to solar glass [11], [15], [26], [27]. A recent year-round study conducted on the correlation between artificial soiling and field soiling in the overall dry environment of Saudi Arabia found that heavy dew tests in the lab appear more predictive of outdoor soiling during the dry summer months, whereas dry and light dew tests followed by wind blow tests align more with soiling behavior in the humid winter months [28]. In this paper, we aim to closely replicate the field soiling losses in a humid subtropical climate by implementing three improvements to our previously established heavy dew soiling methods [15], [26], [29]: (1) using field-specific soil composition and dust concentration levels inside the artificial soiling chamber, (2) applying field-specific dew formation inside the artificial soiling chamber, and (3) using a UV conditioning step (if fresh modules are used) prior to the initiation of artificial soiling and a humidity generation step prior to the soil dispersion step in the artificial soiling sequence.

Using this improved artificial soiling approach, we attempted to replicate the field soiling losses for commercial-size PV modules. We used two different models of PV modules with distinct surface properties, both produced by the same module manufacturer. The modules were first evaluated for soiling loss in a PV installation in the mid-Atlantic region of the United States, and then they were retrieved for soiling loss evaluations before and after artificial soiling in the laboratory. This paper is organized as follows: Section II provides details on the two models/types (MA and MB) of modules used for the experiments, the improved artificial soiling approach, the determination of climatic, and installation/tilt test conditions for soiling. Section III reports the results from artificial soling of two field-retrieved modules (one module per model/type) and one unexposed module with MA model. We discuss the possible causes of the soiling differences between the two models using optical and compositional characterization tools. Section IV summarizes the improvements to the artificial soiling approach and provides insights into the future implications of artificially replicating the field soiling losses on coated glass coupons with different surface properties.

II. METHODOLOGY

A. Test Modules for Field and Artificial Soiling

Two 60-cell commercial modules with two different models (MA and MB) were retrieved from two adjacent PV arrays with identical tilt angles after a 3-year field operation in the mid-Atlantic region of the United States (humid subtropical climate). Adjacent MA and MB fielded modules showed a difference in soiling that was visible to the eye. This difference in soiling was reflected in both laboratory and field measurements, shown in the last two rows of TABLE II. Other module specifications related to these two models are also provided in TABLE II. Both models were produced by the same manufacturer. Both are glass/backsheet laminates, with monocrystalline cells in the first model (MA) and polycrystalline silicon in the second model (MB) as a reference. The sunlit side had tempered glass with an unknown antireflective coating. The module manufacturer did not disclose any information about the antireflection coating or the irregular stipple, which is common in the rolled glass presently used in PV modules. Unfortunately, due to restrictions from the module supplier, the full-sized module could not be cut into smaller samples suitable for use in physical characterization equipment.

The test program contained four modules: three from MA (MA-1, MA-2, and MA-3) and one from MB (MB-1). The MA-1 and MB-1 modules were retrieved from the field, whereas MA-3 served as an unexposed control module and MA-2 was unexposed but stressed under accelerated UV light (total UV dosage of 300 kWh/m^2 at 60°C) to observe whether the high dosage of UV/temperature stress affected the surface properties and corresponding soiling loss levels. To assess the extent of soiling loss of these modules, we conducted short-circuit current (I_{SC}) measurements under natural sunlight on each module using a calibrated reference cell, a thermocouple attached to the backsheet of the module, and a digital ammeter. To correlate the laboratory soiling measurement with the field measurement, we normalized the readings using (1):

$$I_{SC}^{STC} = I_{SC}^{m}\,[1 + \alpha(T^{m} - T^{STC})]\frac{G^{m}}{G^{STC}} \quad (1)$$

TABLE II. INFORMATION ABOUT THE TWO MODELS/TYPES OF MODULES USED IN THE STUDY.

Module Model/Type	**MA**			**MB**
Cell Technology	Mono-Si glass/backsheet			Poly-Si glass/backsheet
Glass	Tempered rolled glass with an unknown antireflective coating on the sunlit side			Tempered glass with possible antireflection and/or antisoiling coating on the sunlit side
Encapsulant	Ethylene vinyl acetate (EVA)			EVA
Rated Power	260 W			235 W
Module ID	MA-1	MA-2	MA-3	MB-1
Exposure Status	Field-exposed	UV-stressed	Unexposed	Field-exposed
Avg. Soiling Loss in Arrays from Field Operation	5.1%	-	-	2.6%
Avg. Soiling Loss (I_{SC}) in Modules from Lab Testing	4.21%	-	-	2.48%

where T denotes temperature, G denotes irradiance, α is the temperature coefficient of the I_{SC}, superscript m indicates the measured condition, and STC indicates standard test conditions (irradiance of 1000 W/m^2, module temperature of 25°C, air mass of 1.5). α was taken from the manufacturer's datasheet; it is 0.04%/K for the MA model and 0.06%/K for the MB model.

The I_{SC} losses for the field-exposed MA-1 and MB-1 modules were determined at two locations: in the field before shipping to the laboratory and at the laboratory right after transportation. The I_{SC} losses of the two field-exposed modules were determined to be 5.2% and 2.6%, respectively (in the field), and 4.21% and 2.48%, respectively (in the laboratory). The resulting ratios of I_{SC} losses between MA and MB models were 2.0 in the field and 1.63 in the laboratory. This minor difference in these ratios is possibly due to (1) loss of contamination during transportation of the modules from solar plant to laboratory, or (2) over- or under-estimate of soiling loss determined by I_{SC} loss compared to power loss, particularly for nonuniform soiling of PV modules in the field [30]. We found that the I_{SC} values of both modules were practically identical (about 3%) after cleaning, indicating that the recoverable I_{SC} losses of the field-retrieved modules exclusively result from soiling and not any other issues, such as variation in encapsulant browning levels. The soiling ratio (SR), as defined in IEC 61724-1 standard [31], is the ratio of the plane-of-array irradiance measured by a soiled sensor (through I_{SC} or maximum power measurements) to that measured by a clean sensor. Soiling level (SL) represents the percentage loss in irradiance due to soiling and is calculated as 1-SR. The soiling level ratio (SLR) used in this study specifically represents a ratio of SLs between the test module (MA) and the reference module (MB) at the module level and cell level in the following artificial soiling tests, as shown in (2):

$$SLR = {1 - SR_{MA}}/{1 - SR_{MB}} = {SL_{MA}}/{SL_{MB}} \quad (2)$$

B. Test Conditions for Artificial Soiling Testing

Our goal in the artificial soiling chamber testing was to closely simulate the site-specific climatic conditions of the soiling months, thereby replicating the natural soiling loss levels. As indicated in the previous section, the tested modules were retrieved from a utility-scale solar plant located in a humid continental climate in the mid-Atlantic United States. The weather data used in this study were obtained from the National Renewable Energy Laboratory's (NREL's) National Solar Radiation Database (NSRDB). The field dust concentration data were sourced from the U.S. Environmental Protection Agency (EPA) [32]. The monthly means of three-year climatic parameters (RH, ambient temperature, dew point, wind speed, and precipitation) are shown in Fig. 1a. The typical RH value was about 76%, and the ambient temperature varied between 1.2°C and 26.9°C. These temperature and humidity conditions resulted in a dew point range from -1.54°C to 20.34°C. Dew tends to assist dust sedimentation after airborne dust particles fall onto the surface due to gravitational settling in a dry period, based on the capillary adhesion strength during moisture-rich periods [33], [34]. PM10 data (see Fig. 1b) indicated a greater dust concentration (12.17 μg/m^3) for June, July, and August than the annual average (9.39 μg/m^3). The deposition process is more notable in June, July, and August; thus, these months are considered the "soiling months" for the site. While the dew point and other meteorological conditions are not constant in the field, the approach to artificial soiling here is to use the average dew point from a representative location to simulate the effect of the morning dew. The regional soiling losses in the soiling months are larger (0.07%–0.09% per day) than in other months (0.06%–0.08% per day) for a PV system with a fixed tilt of 22° based on NREL's soiling map [35]. Because the wind speed is 2–3 m/s in the mid-Atlantic location, dust loss from wind is deemed negligible and is not considered in the study.

Based on the aforementioned historical climatic data for the soiling months, we determined the site-representative soiling environment for the artificial soiling approach as follows: RH of 74% ± 2%, ambient laboratory temperature of 22°C ± 3°C during dew formation period, and no constraints imposed on the RH value during the period of dust cementation/baking at an average nominal operating cell temperature (NOCT) of 46°C. Artificial soiling of the test modules was performed at the same tilt angle (latitude tilt of 38°) as in the solar plant.

C. Artificial Soiling Approach for Commercial Modules

The artificial soiling approach was implemented using a cubic soiling chamber (60 x 60 x 60 cm^3) made of plastic sheets. After removing the bottom sheet, we placed the chamber on top

of the test module, right above the target solar cell. The individual terminals of the target solar cell were accessed at the inter-cell locations by cutting and opening the backsheet. The soiling loss (I_{SC} loss) measurements were carried out using soldered wires, a Glorious-lite 100-W LED lamp (400–750 nm), and a Fluke 87V digital ammeter. The LED lamp gave a solar intensity of 25 W/m^2 over the area of a single solar cell within the test module. The site-representative and soiling-prone environment of the soiling months was achieved in the artificial soiling chamber using temperature and RH controllers. Humidity was generated using a household humidifier until it reached and stabilized at a predefined level. The initial air temperature inside the chamber was maintained at the same temperature as the lab, whereas the temperature of the target cell was controlled and locally maintained at the designated temperatures for dew formation and baking using a portable 3.5-kW air conditioner and a 250-W infrared lamp, respectively. A dew point sensor located near the target cell was used to ensure that the temperature near the glass surface of the target cell was below the dew point, determined from the

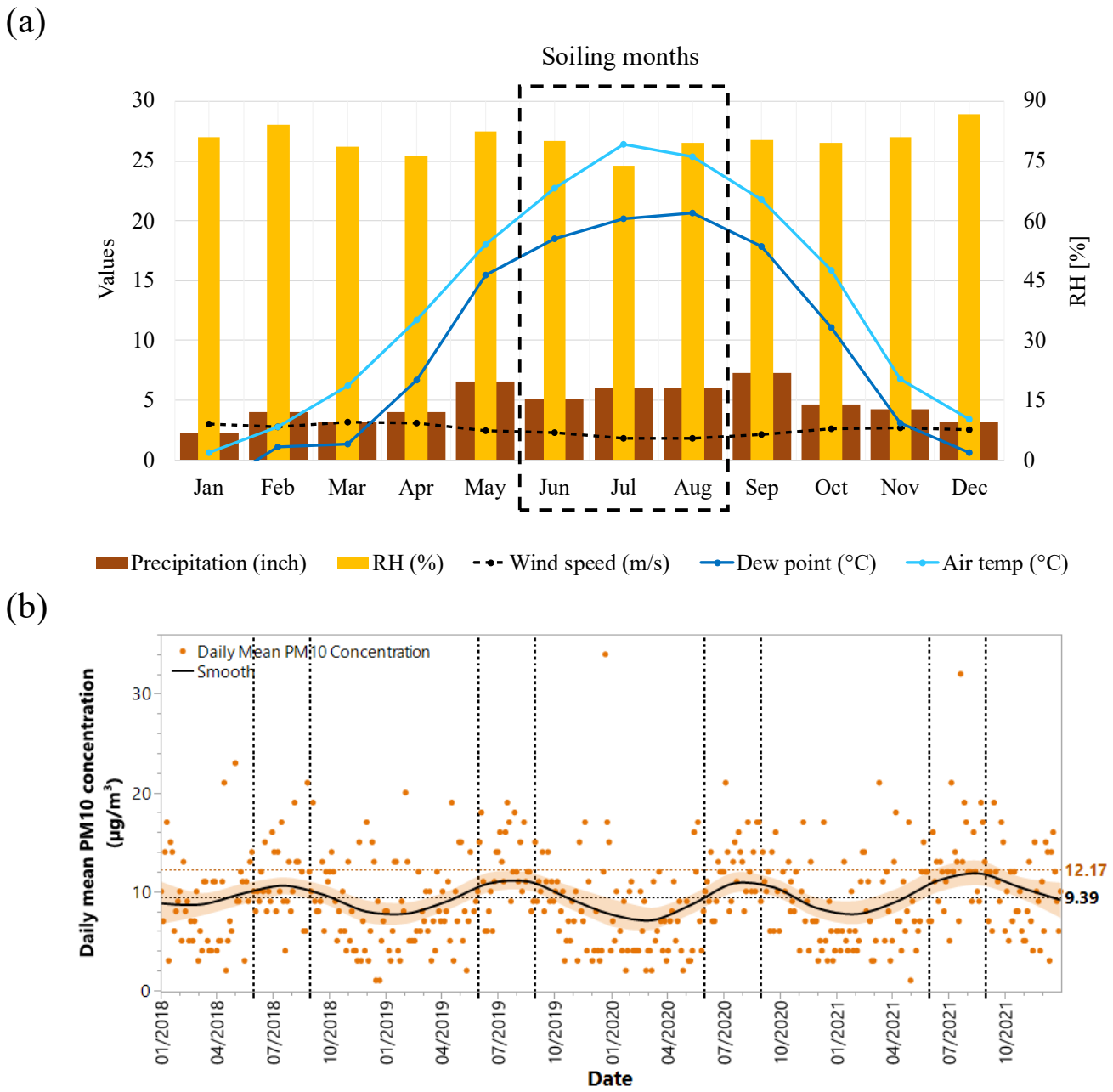

Fig. 1. (a) Monthly average climatic parameters of the site between 2018 and 2021, including ambient temperature (ºC), dew point (ºC), RH (%), wind speed (m/s), and precipitation (inch); and (b) daily mean PM10 concentration. The primary soiling months of June, July, and August (between vertical dotted lines) at the site show a higher average dust concentration level (12.17 µg/m^3) compared to other months. The average annual dust concentration is 9.39 µg/m^3 at the monitoring location near the site.

Magnus-Tetens approximation [36]. The entire module was mounted onto a rotatable aluminum support structure and was latitude tilted for dust accumulation and deposition processes. The dry dust samples were blown from the dust dispenser into the chamber using high-pressure dry air from an air compressor set at 50 psi. The dust samples were injected from the dust dispenser, which was wrapped with an intrinsically hydrophobic Teflon sheet. The weight of the injected dust charge (W_{inj}) was calculated as the weight difference of the dust dispenser obtained before and after dust injection. To maintain 0.1-mg precision and minimize disruptions from ambient air movement, we conducted the weight measurement inside a draft-shielded Radwag WTC-600 digital microbalance. The measured I_{SC} values were normalized to several target dust levels (0.15 g, 0.3 g, 0.6 g, 2 g, and 4 g). The resulting soiling loss for each dust level is defined as the normalized I_{SC} loss, denoted as $\Delta I_{SC,norm}$.

Fig. 2 presents our artificial soiling process flow, which consists of two phases—Phase I: sample conditioning, and Phase II: cyclic artificial soiling implementation. We randomly selected a solar cell from the middle substring of the test module for the indoor soiling experiment to reflect the disproportionate field soiling loss observed in strings of cells within a PV module. The soiling losses of the cell were evaluated after it was placed flat and completely cleaned prior to artificial soiling. This measurement serves as the baseline for subsequent artificial soiling loss comparisons. Each I_{SC} measurement was

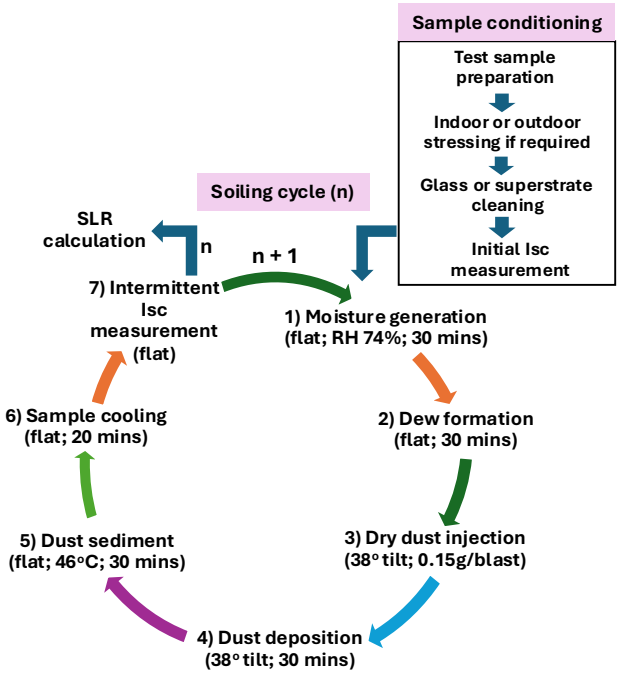

Fig. 2. Artificial soiling approach to replicate mid-Atlantic field-specific soiling. This approach consists of sample conditioning through either indoor or outdoor UV stressing and soiling experiments. Each soiling experiment is composed of (1) chamber humidity generation, (2) dew formation dwell, (3) dry dust injection phase, (4) dust deposition, (5) sample baking for cementation, (6) sample cooling, and (7) I_{SC} measurement for SLR determination.

acquired in the same manner throughout the soiling experiments inside the soiling chamber after cooling the tested cell to room temperature when the module was rotated back to flat. The LED lamp was placed at a square window on the top of the chamber, directly above the cell, to ensure perpendicular illumination. In Phase II, the artificial soiling experiment proceeded through steps 1–7. We started with 30 min of humidity generation to reach 74% RH (i.e., the mean daily RH during the "soiling months"), replicating dew formation at the mid-Atlantic site. Although the mean daily RH was used in artificial soiling here, the maximum daily RH is recommended for future artificial soiling, as it can result in cementation that is more representative of field soiling despite its shorter duration in field PV installations. Although dew formation can happen within the first few minutes, a sufficient amount of moisture on the surface was obtained by fixing a time period of 30 min. During the process of dew formation, the RH inside the chamber was maintained at 74% ± 2%. At this high humidity level, the injected dry dust particles mix with air-suspended water particles and deposit on the glass surface of the target cell at a higher rate than in lower-humidity conditions. Smaller particles with a higher surface-to-volume ratio will absorb more water and settle faster than in drier air [37]. Under dry conditions, the large particles deposit faster (due to gravitational effect) to form the first few layers of soil, but under humid conditions, both large and small particles are expected to combine to form the first few layers of soil. Therefore, we implemented humidity generation in the first step of our approach and used a settling time of 30 min to allow most of the dust particles of various sizes to fall and deposit. The settled dust was baked at the average NOCT value of 46°C, as reported in the California Energy Commission database accounting of ~19,000 modules [38]. At this temperature, baking for 30 min can cause dust particles to become cemented, such that they are likely not able to be removed at typical site wind speeds. Hence, the effect of wind was not investigated in this study. Finally, an intermittent I_{SC} measurement was taken after each soiling cycle, and the intermittent SLR was then determined between the test and reference samples. The uniformity of the artificial soiling developed in the study was examined on an area of 15.6 cm x 15.6 cm, similar to a solar cell, as detailed in Appendix A. With 0.15 g of dust per injection, the soiling nonuniformity remained acceptably small, within 0.25%.

An explanation is warranted for the correlation observed in soiling losses between field and laboratory conditions, despite the difference in deposition patterns—being non-uniform in the field versus uniform in the laboratory. In a series-connected cell string within a module, the short-circuit current is predominantly limited by the most heavily soiled cell. Consequently, achieving a fully and uniformly soiled surface in the artificial chamber is critical for replicating worst-case scenarios, where entire cells experience significant shading. This controlled uniform deposition allows the laboratory setup to effectively simulate the impact of non-uniform soiling observed in the field, thereby ensuring that the measured soiling losses are representative of real-world conditions.

Potential sources of uncertainty in determining soiling loss using the setup include the following: (1) A small amount (no

more than 30%) of dust particles might settle on the chamber walls instead of the cells' glass surfaces after dust injection. This could lead to an underestimation of the actual soiling loss when assuming that the deposited weight equals the injected weight. This effect would impact all soiled modules equally under the same setup; thus, the resulting SLR between the two studied models would be minimally affected, if any. Nevertheless, an accurate measure of deposited dust on the tested cell is necessary for a quantitative correlation. (2) LED light sources are known for their instability and lack of repeatability due to operating temperature variation. To mitigate this, we manually cooled the LED lamp to room temperature before each soiling loss measurement and completed the measurements within 3–5 seconds to minimize temperature-induced irradiance instability. However, the low irradiance levels produced by the LED, due to the considerable distance (60 cm) between the lamp and the cell, may not sufficiently detect irradiance variations. Therefore, using a lamp source from a solar simulator is preferable, and verifying the lamp's irradiance with a calibrated reference solar cell prior to measurement is recommended in future studies.

D. Characterization Techniques

In addition to the I_{SC}-measured soiling loss evaluation technique, we also used other soiling-relevant nondestructive characterization techniques to help identify the factors that reduce light transmission through coated cover glass and encapsulants. UV fluorescence (UVF) imaging was used to visualize encapsulant degradation and to visually observe the color differences between dust samples, and a colorimeter was used as a color change index to quantify light absorbance in the visible range. The former provided qualitative evidence for the extent of EVA browning, whereas the latter quantitatively evaluated transparency changes in the cover glass and encapsulant layers.

As mentioned in the Methodology section, the I_{SC} values of both field-retrieved modules were nearly identical after cleaning, indicating that the observed change in I_{SC} after cleaning was exclusively related to soiling rather than variation in encapsulant browning levels (as confirmed via UVF imaging, not shown here). Two types of dust samples were used in the artificial soiling experiments: field dust and ISO 12103 Arizona Road dust. Field dust was collected from the glass surfaces of the field-exposed modules retrieved from the site. A Bruker S2 PUMA energy-dispersive X-ray fluorescence (XRF) spectrometer and a Microtrac model 3500 laser diffraction analyzer (LDA) were used to measure the chemical composition (excluding organic matter) and particle size distribution of the dust samples, respectively. The color of the dust samples was also examined using a colorimeter, as a correlation between dust color and certain minerals in the dust samples has been observed in the literature and verified here.

The coating film and glass texture are critical parameters to consider when interpreting field soiling results, as they can be influenced by changes in coating thickness and material decomposition during aging. We investigated the air-side coating film on the glass surface using Fourier transform infrared spectroscopy (FTIR), which is intended to detect the presence of any coating or chemical changes in the coating materials. Microscopic images of organic matter on the cover glass revealed possible sources of field dust, which could help explain the causes of the soiling variations. The reflectance spectra in the UV-VIS-NIR range (350–1800 nm) were also obtained at the cell center for all four modules, using a handheld ASD FieldSpec 4 wide-resolution field spectrophotometer after calibration to a reference reflectance spectrum using a white calibration plate. A fiber-optic contact probe was vertically positioned at each measurement spot (3 cm^2) on the glass surface of the tested cell. Lights from a built-in light source into a cone-shaped solid angle with a divergence half-angle of 8° and a detector were positioned to capture reflected light at a 25° angle. In comparison, a PV panel operates at an approximate acceptance angle of ±60° [39].

III. RESULTS AND DISCUSSION

A. I_{SC} Loss and Artificial Soiling Loss Ratio

In the improved artificial soiling experiments, the dust types and amounts used in each soiling cycle were changed and controlled while all other factors remained fixed. We tested

TABLE III. ELEMENTAL COMPOSITION OF FIELD DUST AND ISO 12103 A2 DUST SAMPLE DETERMINED BY XRF ANALYSIS, RELATIVE TO THE MANUFACTURER'S TYPICAL CHEMICAL CONTENT. THE TOP SEVEN ELEMENTS, BY WT%, ARE LISTED IN THIS TABLE. "ND" DENOTES "NOT DETECTED" AND "NM" DENOTES "NOT MENTIONED."

Element	Weight Percent (wt%)		
	Field Dust	ISO A2 Dust	ISO AZ Dust [40]
Si	4.92	62.12	69–77
Al	ND	11.38	8–14
Fe	52.8	8.28	4–7
Ca	16.86	7.2	2.5–5.5
K	8.23	6.4	2–5
Na	ND	0.69	1–4
Ti	3.17	0.81	0–1
Cr	1.81	<0.4	NM
Mn	1.08		
Substance density of dust in g/cm^3	4.95	2.62	2.22–2.97

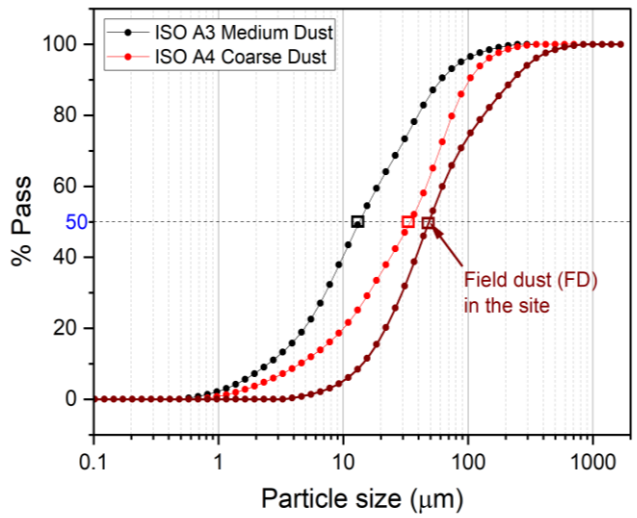

Fig. 3. Dust particle size distribution from LDA for the dusts in this study: field dust from the site and ISO standard A3–A4 dusts. Squared points denote the median particle size (50th percentile) for each dust sample.

three types of dusts—field dust and two types of ISO 12103 Arizona Road dusts (A3 medium dust and A4 coarse dust, collectively referred to as ISO dusts)—using five different charge weights for each (0.15 g, 0.3 g, 0.6 g, 2 g, and 4 g) in more than 20 soiling cycle experiments. The field dust samples were manually collected, using a stiff paper sheet, from the glass surfaces of representative modules retrieved from the site. The samples collected contained large particles with irregular shapes as well as with fine, non-sandy, dark brown particles. By the time of collection, the largest (and least adhered) particles might have been lost in transport and handling, whereas the smallest (and most adhered) particles and water-soluble species might have remained bound to the glass surface. They were then filtered through a standard #40 dust sieve with an opening size of 425 microns to remove large and localized content such as bird droppings. The ISO dusts were laboratory-made and purchased from Powder Technology Inc. TABLE III shows the elemental composition, in weight percentage (wt%), obtained using LDA for both the field dust sample and the ISO dust samples. A2 dust, obtained from the same manufacturer as the A3 and A4 dusts, where the same material is sieved to a smaller size distribution, was examined early in the study. The composition of field dust differs remarkably from that of the ISO standard dusts. In ISO dust, silicon is predominant, at 62.12 wt%, with a dust density of about 2.62 g/cm^3, similar to the standard composition of ISO dust reported in [40]. In contrast, field dust collected from the module surface at the site is greatly enriched with iron at 52.8 wt%, with a dust density of about 4.95 g/cm^3. The iron, in its oxide form with active absorptance bands at UV and visible range [41], [42], [43], has higher sunlight absorption compared to silicon in its oxide form. This difference in the light absorption spectrum is expected to make a significant difference in the extent of soiling loss for identical soiling layer thicknesses of these two oxides [44], [45]. The substance densities of the dust samples were roughly estimated using the wt% of each element and the known densities of these elements. Fig. 3. shows that over 95% of field dust particles are larger than 10 microns, with the median particle size (50th percentile) at 48.49 microns. In comparison, ISO dusts contain a higher proportion of finer particles, with median diameters approximately 11–22 microns for A3 dust and 34.56 microns for A4 dust. Therefore, ISO A4 coarse dust is closer to field dust in terms of particle size distribution. In the near-wet deposition mode, the impact of particle size on deposition rate may be less pronounced. Therefore, to closely replicate the field environment in the study, it is important to introduce the humidity step prior to the dust dispersion step, as the soil deposition rate is an interplay between particle size distribution, dust density, and humidity level (moisture absorption).

Fig. 4 shows the normalized I_{SC} loss ($\Delta I_{SC,norm}$) and SLR after each dust deposition. For the field dust (see Fig. 4a), the SLR value decreases from 1.63 to 0.98 as the amount of soil per injection increases from 0.15 g to 4 g. This trend indicates that the highest SLR value, which is closest to the field SLR values (approximately 2x), occurs when the soil amount per injection is the lowest. Although field soiling in various climates typically involves slow accumulation and gradual layering of dust on module glass surfaces, this study revealed that reducing the initial dust layer deposition most gives the greatest effect on optical performance. Although the initial quantity of the first thin dust layer was not directly explored here, it appears to be a direct response to the surface properties, climate, environment, and installation factors, and it appears to remain practically unaffected by subsequent layers, as the bonds between dust particles are relatively weak compared to the bonds between dust particles and a wet surface. Fig. 4 shows the systematic difference observed between field dust (where a greater loss of I_{SC} is observed for MA) and ISO dust (where a greater loss of I_{SC} is observed for MB). Such a difference may result from the characteristics of the separate dusts (particle size distribution and composition) as well as their propensity to stick to the different surface coatings.

The I_{SC} loss is more pronounced after a single thin-layer injection (23% loss per gram at 0.15 g) than at multiple-layer injection conditions (8% loss per gram at 4 g), as shown in Fig. 4a. However, the relationship between loss per gram and the dust amounts is not constant, particularly for small dust injections (e.g., <0.6 g). For larger dust amounts, e.g., >0.6 g, it becomes an approximately constant value, as the I_{SC} loss increases nearly linearly with the total quantity of dust injected. A more attenuating soiling layer at lower dust injections suggests that more light is attenuated due to a thicker dust layer formed after multiple injections. The linear effect on optical performance (and I_{SC}) is less definitive, particularly for the artificially soiled MA-1 module using field dust. This can be effectively modeled using the Hegazy model derived from field soiling data, as shown in Appendix B. At lower dust concentrations, a linear relationship between dust mass and optical performance (and I_{SC}) is generally applicable. For the MA-1 module artificially soiled with field dust, the initial dust deposition had a more significant impact on optical transmittance compared to subsequent layers. This is likely due to the complex interplay of light scattering, absorption, and dust adhesion behavior on the glass surface. A similar nonlinear

trend of I_{SC} loss with injected dust during artificial dust buildup with wind conditions of 0.63–3 m/s was seen in [46]. The soiling experiment within a chamber in an air-conditioned room may still involve gentle air turbulence.

(a) Field dust

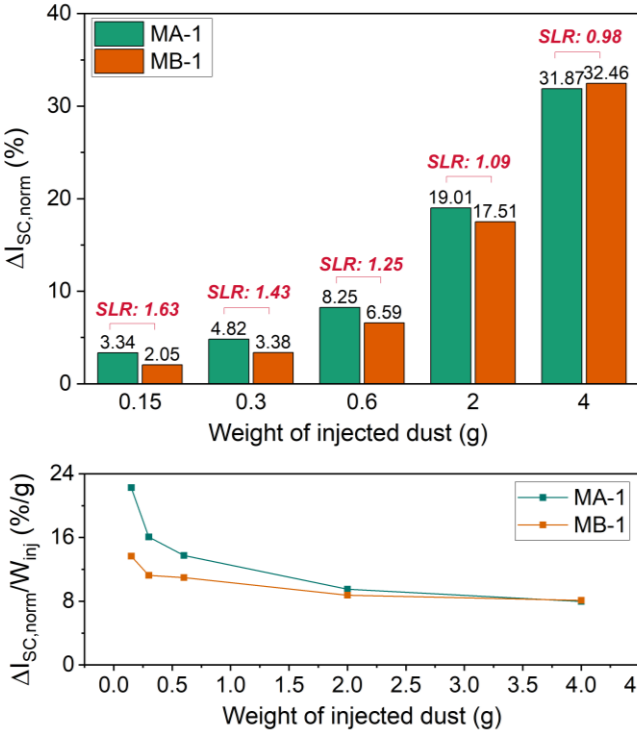

(b) ISO 12103 A3 dust

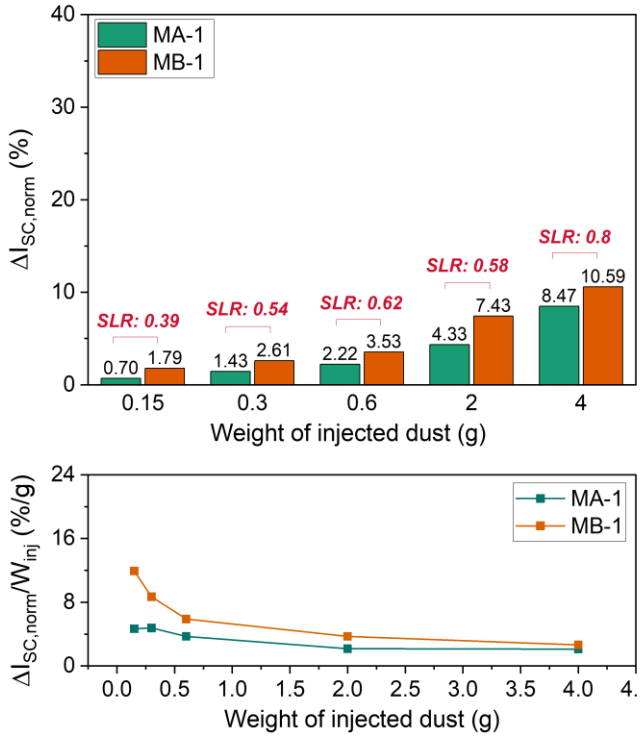

(c) ISO 12103 A4 dust

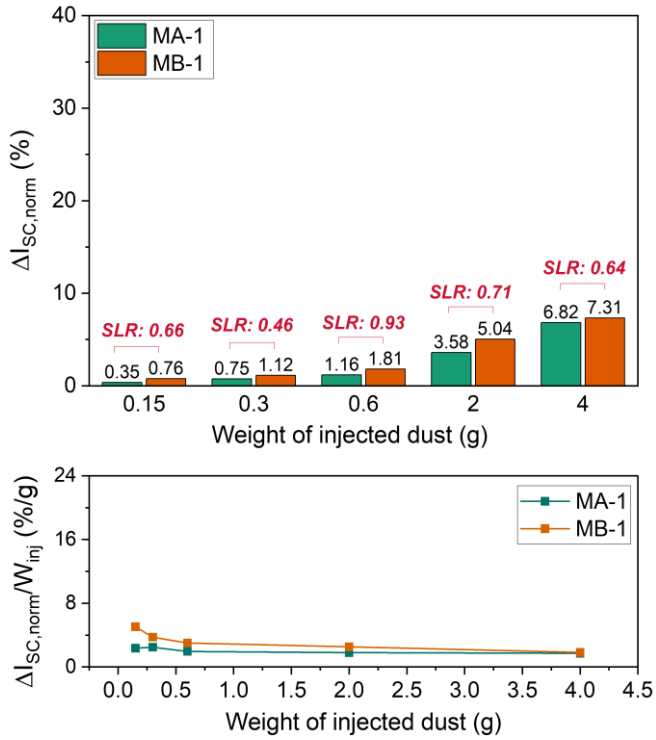

Fig. 4. The normalized I_{SC} loss ($\Delta I_{SC,norm}$) with resulting artificial SLRs (bar plot, top) and the loss per injected weight ($\Delta I_{SC,norm}/W_{inj}$) (line plot, bottom) using various dust amounts and types: (a) field dust, (b) ISO A3 dust, and (c) ISO A4 dust. The injected dust amounts (W_{inj}) are close to 0.15 g, 0.3 g, 0.6 g, 2 g, and 4 g.

Compared to the field dust, significantly lower soiling loss were observed for the ISO A3 and A4 dusts (see Fig. 4b–c). This could be attributed to a larger amount of lower-density but larger-diameter particles in the field dust, such as organic matter, covering more surface area compared to the ISO dust type. The iron oxides in field dust are known for being densely packed and can form aggregates or clogs more readily than sand-dominant ISO dusts, resulting in a dense dust layer that effectively masks the glass surface. Furthermore, the difference in dust adhesion between the two models of modules was closely linked to the variation in surface properties of the glass between the models, which were not measured but are indirectly discussed in the following sections.

B. Effect of Surface Properties of Glass

This section and the following ones present the possible causes of the soiling loss differences between the two models using a few nondestructive characterization techniques.

In an FTIR infrared spectrum, the peak position is dictated by the specific vibrating functional group or molecular bond in the surface coating, and the peak height and area are proportional to the quantity of that functional group or bond. We used FTIR to determine whether there were any significant differences in the chemical compositions of coating materials among the studied MA and MB models under varying

conditions. The infrared absorption spectra obtained using an Agilent 4300 handheld FTIR spectroscope are shown in Fig. 5. An attenuated total reflection (ATR) diamond crystal was placed on the glass surface of each location for FTIR measurements. The measurements were taken at 6–7 different randomly selected locations above the cell areas of the test modules. The peak positions from both models were identical at 901 cm^{-1} (associated with the Si-O-Si bond) and 756 cm^{-1} (associated with the Si-OH bond) with and without field exposure or accelerated UV stress testing. This indicates that within the measurement range, there is no difference in the functional groups of the coating layers among models. There is less spatial variation seen in the infrared characteristics of the coating material at varying positions on the MB model. UV stressing can reduce the infrared absorption of the two major peaks of the UV-stressed MA model (MA-2); however, there are considerable overlaps in the spectrum between the unexposed MA module (MA-3) and the field-exposed MA module (MA-1). It remains unclear whether the compositional degradation of the surface coating occurred during field exposure.

C. Effect of Dust Chemistry

The color of dust samples can signify the chemical composition. As shown in TABLE IV, field dusts appear to be dark brown, whereas the ISO standard A3–A4 dusts appear to be light brown. To compare to the literature, we calculated the redness index (RI) for each dust sample using the following formula: $RI = \frac{L\cdot\sqrt{((a^*)^2+(b^*)^2)}\cdot 10^{8.2}}{b^*\cdot L^6}$, where L is the lightness and a^* and b^* are two chromaticity coordinates in CIELAB color space [47]. These chromaticity values were measured by placing thick, compacted dust samples onto a white backsheet using an X-rite Ci6X colorimeter. This calculation helps estimate the hematite content, which is a common iron oxide compound in soils. Previous studies have demonstrated that a larger RI correlates with a higher hematite content, and there is a linear relationship between the two [48], [49]. Indeed, the RIs measured from the two field dust samples on MA and MB modules were 10 and 6.3, respectively—significantly higher than the 0.22–0.33 values obtained for ISO standard dusts. This indicates a substantial presence of iron oxide in the field dust, aligning with the XRF data shown in TABLE III. Additionally, we observed in the UVF images that ISO dusts emitted a reddish fluorescence when exposed to UV light, whereas field dust particles did not show any fluorescence. The reddish shining particles in the ISO dusts are likely from silica, as reported in [50]. UVF imaging can be used as a quick tool to qualitatively identify the compositional differences between the field and standard dusts.

In addition to iron oxides, the field dust on the module surface likely contained organic materials, such as fungi and bird droppings, as shown in Fig. 6. Visible images at four different positions (a–d) on the glass surface show a variety of organic materials. Microscopic images taken at each spot revealed fungi similar to those reported in a previous study by Toth et al. [51]. In their study, various fungi were seen on field-exposed full-size PV modules from an installation in Germany. Other organic contents, such as bird droppings, were also present in the field dust and could potentially reduce light transmittance. According to Wiesner's research, organic materials like pollen grains exhibited significantly larger adhesion force to the glass surface and thus enhanced particle attachment [52]. Because organic content can be present in field dust, field dust chemistry is critical for closely replicating field soiling in the indoor artificial soiling approach. Field dust is unfortunately often limited or unavailable for indoor soiling experiments. Customized field-specific, laboratory-made dust could serve as a practical alternative, allowing for the inclusion of diverse components such as salt, fly ash, clay, volcanic debris, soot from forest fires, and carbon black.

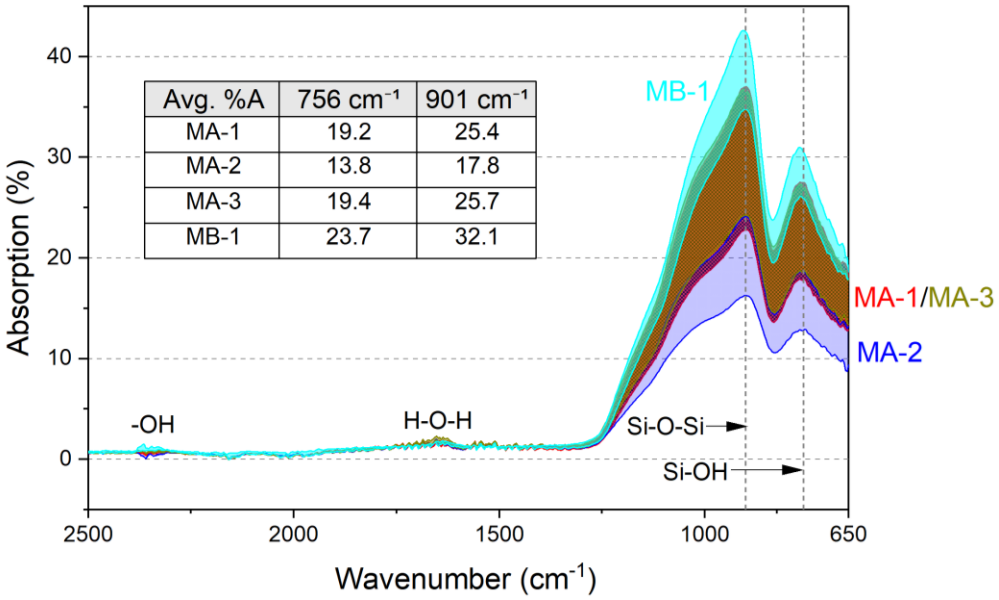

Fig. 5. ATR-FTIR absorption spectra of glass surfaces from three MA modules and one MB module. The spectra from 6–7 different positions on each module are shown as areas. Major transmittance changes are seen at 901 cm^{-1} (associated with the Si-O-Si bond) and at 756 cm^{-1} (associated with the Si-OH bond). Average absorptances (Avg. %A) are given in the table for the two major absorption bands.

TABLE IV. VISUAL IMAGES OF FIELD DUST AND ISO STANDARD DUSTS—FOUR SAMPLES WITH AN IDENTICAL WEIGHT OF 1.507 ± 0.0002 G. DUST SAMPLES INCLUDE: #1 (FIELD DUST FROM MA-1 MODULE), #2 (FIELD DUST FROM MB-1 MODULE), #3 (ISO A3 MEDIUM DUST), AND #4 (ISO A4 COARSE DUST). RI AND UVF IMAGES OF EACH DUST SAMPLE ARE ALSO GIVEN.

	#1 Field Dust from Module MA-1	**#2 Field Dust from Module MB-1**	**#3 ISO 12103 A3 Medium Dust**	**#4 ISO 12103 A4 Coarse Dust**
Visual Image	RI = 10 	RI = 6.30 	RI = 0.31 	RI = 0.22 
UVF Image	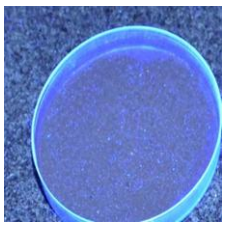	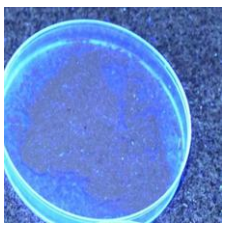		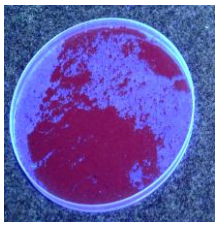

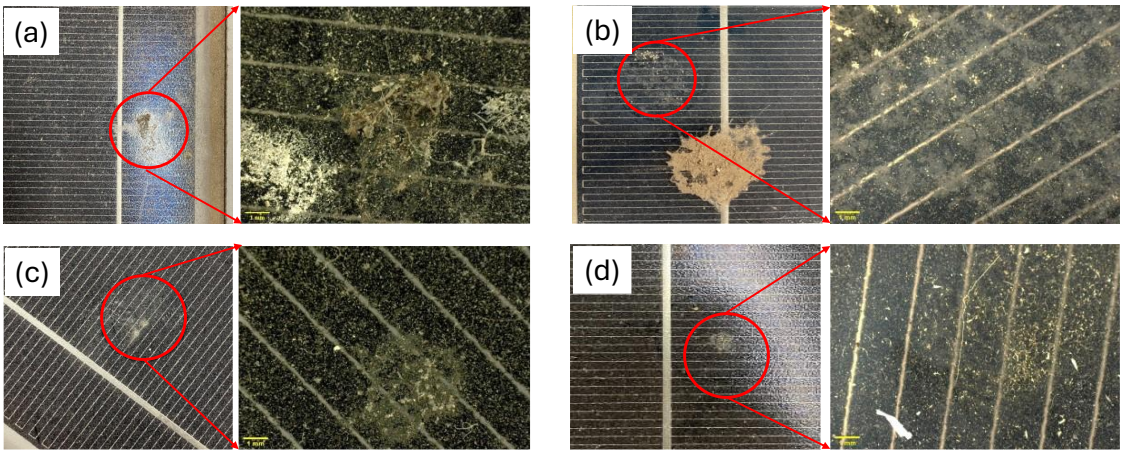

Fig. 6. Optical images and micrographs of organic materials found on the glass surfaces of the field-retrieved modules (MA-1 and MB-1). Possible sources of the organic materials are fungi and bird droppings. The magnification of the micrographs is 30x.

A series of reflectance spectra across the UV, visible, and infrared range may be used to derive the content of the organic (soil organic carbon, or SOC [53]) and mineral (iron oxides [54], [55] and clay [56]) components in soils. Fig. 7 shows the mean optical reflectance (averaging ten measured spectra, R_m) and the continuum removal (CR) reflectance spectra [57] for glass coupons soiled using four dust samples (ISO 12013 A3, ISO 12013 A4, field dust from module MA, and field dust from module MB). The CR reflectance spectra were computed in ViewSpec Pro software as $(R_c - R_m)/R_c$, where R_c is a convex hull fit to the spectrum R_m. The convex hill fit accentuates the absorption bands in the spectra while minimizing the effect of the background spectrum resulting from differences in illumination and view geometry [58]. For the mean reflectance spectra (see Fig. 7a), the ISO dusts were characterized by higher reflectance across the measured wavelengths between 350 nm and 1800 nm because they contained high-reflectance minerals, including quartz and calcite. The two field dust samples had similar reflectance spectra, both showing lower reflectance through the measured wavelengths. The field dust is believed to contain more optically absorbing minerals like iron oxides and/or soil organic content, as demonstrated in the literature [59], [54] and in the aforementioned results from other characterization techniques. The corresponding CR reflectance (see Fig. 7b) in the visible range (350–580 nm) could indicate iron oxides [60] in the field dust. The infrared wavelengths associated with hematite and goethite often occurred separately, at 848–906 nm and 909–1022 nm, respectively [61]. However, the presence of these iron oxides was difficult to isolate in the infrared spectral region due to band overlap between iron oxide absorption and broad absorption due to organic matter, as in [59].

The detection of organic particles using reflectance spectroscopy is limited here because the absorption bands for carbon-containing organic matter typically occur at longer infrared wavelengths [62]. Another absorption band in the visible range (550–700 nm, given in [59]) was seen in the field dust samples, especially the one collected from the MA-1 module. Compared to the MB-1 sample, the dust sample associated with the MA-1 module absorbed slightly more light in the measured spectral range.

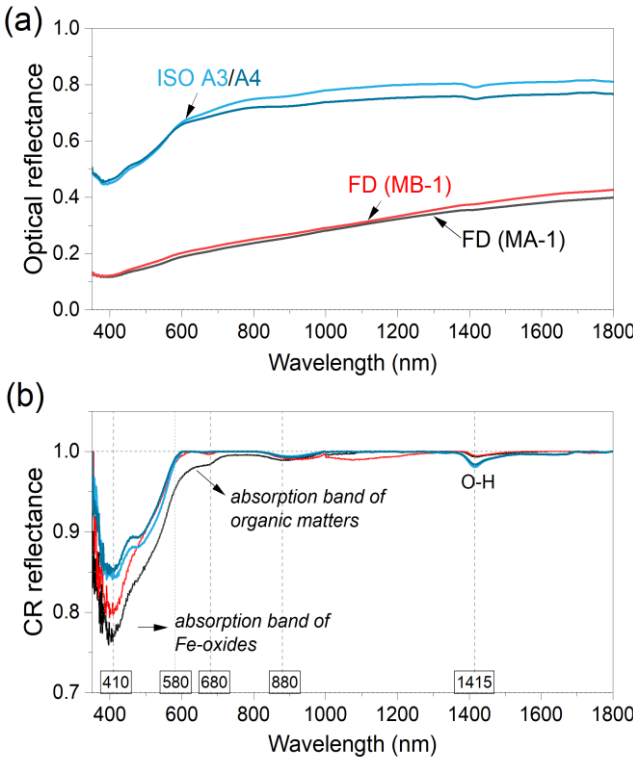

Fig. 7. (a) Optical reflectance spectrum and (b) continuum removal (CR) reflectance spectrum of four dust samples, including ISO 12103 A3 and A4 dusts and field dusts from each MA-1 and MB-1. The wide absorption bands between 350 nm and 580 nm may indicate the presence of iron oxides, and another band centered at 680 nm may indicate organic matter in the field soil samples.

D. Effect of Accelerated UV Stress on Glass Surface Coating

To study the optical reflectance of the glass alone, without the influence of the PV cells and backsheet from the two models, we removed (melted using a soldering iron) the backsheet in the noncell regions between cells in the two modules and measured the reflectance (see Fig. 8) on the MA or MB glass located above an old-type Siemens M55 solar cell. The MB glass, compared to the MA glass, showed higher reflectance across the UV-VIS-NIR range. In contrast, the greater reflectance of the MB may result from an optically lossy antisoiling coating, possibly in addition to the absence of an antireflective coating. Because an integrating sphere was used, the effect of the glass layer's roughness on light reflectance was limited; however, optical backscattering may occur from the field dust, which was not assessed in the study.

In addition, the coating applied on a glass surface may undergo a constructive curing process under a small dosage of UV irradiation in the sunlight. As an example, when exposed to a 1 Wh/m^2 dose of UV light (365 nm), TiO_2 coatings become superhydrophilic, facilitating water spreading on the coated surface, which in turn helps remove dust particles [63]. To study the effect of UV on the MA coating materials on the cover glass, we performed artificial soiling on the UV-stressed modules using three types of dust (field dust and ISO A3 and A4 dusts), as shown in Fig. 9. Due to the limited amounts of field dust, the experiments were run at dust weights of 0.15 g, 0.3 g, and 0.6 g, respectively. The I_{SC} losses of the field-dusted, UV-stressed module at the three dust levels were higher than those of other dust types on the same module. We believe that this does not reflect an experimental artifact but rather highlights the optical differences caused by the chemical composition (low band gap iron oxide-rich vs high band gap silicon oxide-rich), particle size and physical surface adhesion behavior of the various dust types, rather than just the density of the dust. Without additional measurements using the field dust on the UV-stressed MA-2 module shown in Fig. 9, data extrapolation in any form (any model) is not recommended. Furthermore, although the soiling loss of the field-retrieved

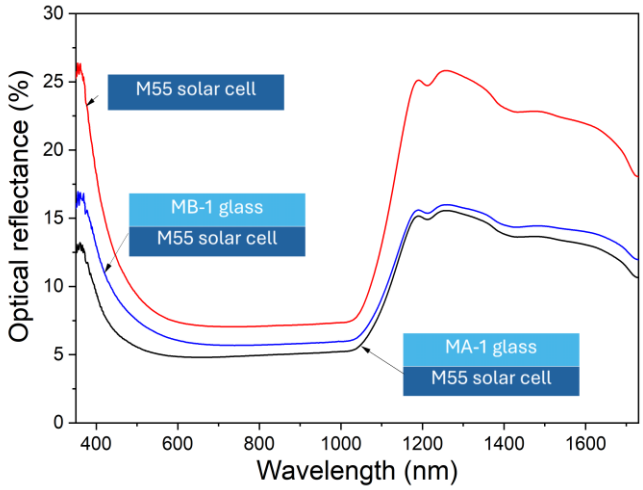

Fig. 8. Optical reflectance spectra of MA or MB glass layer located over an old-type Siemens M55 solar cell.

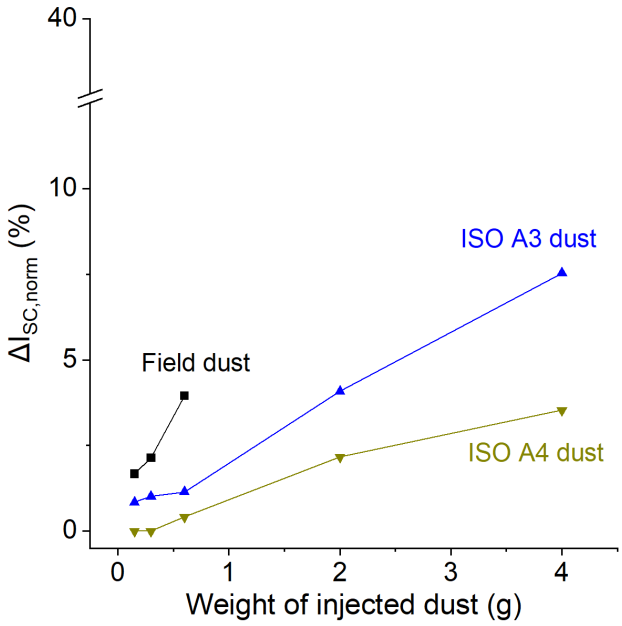

Fig. 9. Normalized I_{SC} loss ($\Delta I_{SC,norm}$) from artificial soiling on the UV-stressed module (MA-2) with Y-scale comparable to Fig. 4. The ISO dust data were collected for five dust injections, and the field dust data were collected only for three dust injections due to insufficient dust availability as explained in the paper.

MA-1 module (see Fig. 4a) is greater than that of the UV-stressed MA-2 module (see Fig. 9) subjected to field dust artificial soiling, the glass surface properties (coating and texture) are not differently affected by artificial UV radiation relative to field aging [64]. The contact angle and roll-off angle, which are more difficult to measure on a PV module, are recommended to characterize the integrity of the surface coating based on its surface energy in future studies. Another cause might be the high-humidity and high-temperature environment, like the studied climate, which can activate curing of any uncured deposited coating. This can lead to a gradual deleterious effect on the surface hydrophobic properties [65]. Even if UV is not a long-term degradation factor in aging the coating on the MA glass surface, we still recommend performing UV conditioning of the test samples before initiating the artificial soiling cycles, as shown in the process flow in Fig. 2. For instance, a greater UV dose (e.g., 300 kWh/m^2, as in [66], or 4000 h of IEC TS 62788-7-2 method A3 [67]) on module or glass coupons to test UV-sensitive coating materials could be applied using a 2-month indoor accelerated UV stress test, which corresponds to approximately 11 years of field dose. Or, a short UV preconditioning (e.g., 15 kWh/m^2, as in IEC standard 61215 [68]) could be used for a 40-day equivalent field exposure.

E. Dust Concentration and Acceleration Factor of Artificial Soiling

The artificial soiling process used in this study, as illustrated in Fig. 2, simplifies and accelerates the natural soiling process by replicating major soil deposition processes but forgoing the dust removal processes (e.g., wind and rain), which are difficult

to reproduce. The soiling loss directly depends on dust concentration in the field or inside an enclosed chamber during each dust injection. As demonstrated in Fig. 4, the level of dust concentration inside the chamber is a critical parameter for closely replicating the field soiling loss.

The daily mean PM10 concentration during the soiling months in the studied region was 12.17 µg/m^3, as given in Fig. 1b. Considering that 95% of the dust particles are larger than PM10 and assuming an identical particle mass and size distribution, as shown in Fig. 3. the combined daily concentration of PM10 and larger particles is estimated to be 243.4 µg/m^3 (without the subsequent effects of cementation). For each dust injection of 0.15 g in the 0.33-m^3 chamber used in this study, the concentration acceleration factor (CAF), a ratio between the maximum dust concentration in the artificial chamber and the daily dust concentration in the field, is about 1900. A large CAF runs the risk of false results because the rate of accumulation is not linear in the field, nor are the factors enabling surface adhesion. Reducing the CAF can be achieved by either decreasing the dust weight or increasing the chamber size. Fig. 10. provides the artificial dust concentration as a function of the cubic chamber size and the dust weight per injection. Obtaining a CAF of 1, i.e., exactly simulating daily soiling loss in the field (0.07%–0.09% per day in a soiling month), required a soiling chamber as large as 8.5 x 8.5 x 8.5 m^3 with 0.15 g of dust per injection, which is practically difficult in conventional research laboratories. CAF can also be reduced by using less than 0.15 g of soil, but researchers will be challenged with measurement accuracy and uncertainty, which are intrinsically related to measuring low weights in microbalances and injecting small amounts inside the chamber. In addition to reducing the CAF, an aerosolizing device can be used to improve the uniformity of dust dispensing, as in VDI 3956 [69]. Therefore, the chamber may be appropriate for desert regions with significantly higher soiling rates, e.g., 1% per day. For the test site, simulating monthly, instead of daily, soiling losses using the current chamber size with 0.15-g soil injection seems more realistic.

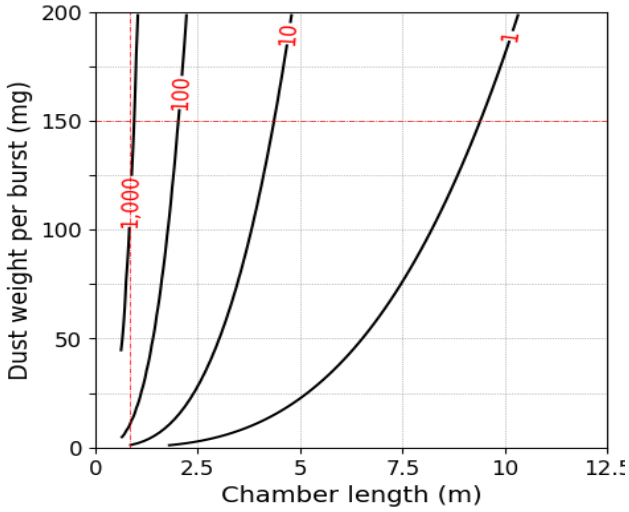

Fig. 10. Contour plot of artificial dust concentration in the chamber, varying with the dimensions of the cubic chamber and the amount of injected dust. The contour lines represent CAF values of 1, 10, 100, and 1000. The dust weight (150 mg) and cubic chamber size (60 cm per side) used in the study are marked with red dotted lines.

IV. CONCLUSION AND FUTURE WORK

In this paper, we have attempted to demonstrate the replicability of field soiling observations of commercial-size PV modules through several artificial soiling experiments conducted in an environmentally controlled soiling chamber. The experiments involved two models of commercial-size PV modules, MA and MB, operated side by side in a solar plant located in a subtropical humid climate. Field operation data revealed that the MA modules experienced nearly twice the soiling losses as the MB modules, despite sharing identical climatic, installation configuration, and cleaning histories. To closely replicate this field SLR using artificial soiling, we meticulously selected and implemented many steps in the artificial soiling method, including: (1) selecting the field-specific soil type and dust concentration level inside the artificial soiling chamber that effectively represent field conditions; (2) selecting a field-specific dew formation condition inside the artificial soiling chamber (RH and baking temperature); and (3) implementing the UV preconditioning step (if fresh modules are being used) prior to the initiation of artificial soiling and implementing the humidity generation step prior to the soil dispersion step in the artificial soiling sequence. These carefully selected and implemented steps allowed us to replicate the field soiling (SLR of 2.0) using artificial soiling (SLR of 1.63). This study clearly demonstrates that the dust type and concentration inside the chamber play critical roles in artificially replicating the average soiling level of a PV module. The methodology presented in this work can be used for rank ordering of different antisoiling coatings developed by different vendors for diverse climatic conditions. A demonstrative rank ordering study is presently underway at our laboratory.

Future improvements to fully evaluate the ability of the developed artificial soiling approach to replicate field soiling effects may include the following: (1) Contamination of all compositions and sizes should be collected from the field. (2) Sufficient dust samples should be obtained to replicate the role of selective adherence of specific particles seen in natural soiling and to investigate the effects of coating weathering (e.g., UV exposure) on coated glass surfaces. (3) Seasonally active deposition mechanisms for other climates should be considered. (4) Repeatability testing should be conducted, ensuring a maintainable and duplicable artificial soiling environment in a specific climate to achieve statistically confident results for intrinsically variable field soiling. (5) Dust uniformity could be further improved, and the actual deposited weight on the surface of the target solar cell relative to the charge of injected dust during the dust deposition step should be accurately quantified by integrating the current soiling chamber with aerosolizing devices and gravimetric samplers. (6) Finally, I_{SC}-based soiling loss measurements should be improved using an LED solar simulator lamp with high stability.

APPENDIX A: ARTIFICIAL SOILING UNIFORMITY IN THE CHAMBER

To assess the uniformity of artificial soiling depositions on an area of 15.6 cm x 15.6 cm (equivalent to the area of one cell in a commercial module), we performed a soiling uniformity check at 16 sites across a 44-cm x 36-cm bare glass sample. Outdoor transmission (%T) measurements on soiled glass samples were taken at total normal irradiance using natural sunlight at around AM 1.5 by placing a calibrated reference cell (2 cm x 2 cm) beneath the test samples with and without soiling. The two readings given by an ammeter were used to calculate %T at each position. For the soiled sample, 0.16 g or 2 g of ISO 12103 A3 dust was artificially deposited under a condition with 74% RH and 38° latitude tilt. Fig. 11 shows the changes in %T of the glass sample under the clean and two soiled conditions. The spatial variation in % was assessed by interpolating the sixteen measured values and estimating the differences from the average %T at each spot. In the clean condition, the differences were within ±0.5% across the entire glass area and within ±0.2% in the single-cell area (dotted region). In the studied single-cell area, the differences in %T remained relatively small, within ±0.25%, due to the low amount of dust deposition (0.16 g) on the glass surface. When 2 g of soil was injected, the nonuniformity in measured %T increased to within ±1.2% in the studied single-cell area. To reduce the non-uniformity in artificial soiling, a larger soiling chamber is preferable, or the amount of dust used in each deposition process should be minimized. We recommend using as little as 0.15–0.16 g of dust in artificial soiling experiments to limit the nonuniformity issue.

APPENDIX B: EMPIRICAL FITTING BETWEEN I_{SC} LOSS AND DUST CONCENTRATION

The appendix is to examine whether linear fitting trends between I_{SC} loss (%) and dust concentration (g/m²) can be universally observed across both low and high dust injection cases. Fig. 12 shows the empirical fitting results using measured data points from Fig. 4 on (a) the MA-1 module and (b) the MB-1 module. The fitting is based on Hegazy model [70], which was developed using field soiling data obtained from middle region of Egypt that relate transmission loss to dust concentration. The model can be described as (3):

$$\left(1-\frac{\tau}{\tau_{clean}}\right)\% = d_1 \cdot \mathrm{erf}\left(d_2 \cdot \omega^{d_3}\right) \quad (3)$$

here, τ is light transmittance at dirt or clean condition, ω is dust concentration in g/m², erf is gauss error function, coefficients d_1, d_2 and d_3 are three fitted parameters. Normalized I_{SC} loss was used to represent transmittance loss.

Hegazy found that the rate of transmittance reduction is relatively higher at lower dust deposition. In fact, as dust deposition increases, transmittance reduction increases with a progressively decreasing rate until reaching its upper limit of 100%. The fitting using the Hegazy model allows a close fitting throughout small to high dust concentration conditions. Other models based on exponential, logarithmic, linear, and polynomial relationships have also been derived by others from field soiling data [71]. From these models, the soiling effect at low dust concentrations (e.g., <1 g) is often approximated as linear. However, no universal linear trend applies across all dust injection conditions. Therefore, we do not recommend performing local fitting using limited data points from injected dust masses below 1 g for each dust type in this study.

ACKNOWLEDGMENTS

The authors would like to thank Dr. Ingrid Repins and Dr. Lin Simpson of NREL for providing valuable guidance and sharing thoughtful input during project implementation and execution. We also thank Akash Kumar, Venkata Sai Tanay Kosaraju, and Abhishek Brahma of ASU PRL for helping prepare some of the artificial soiling experiments. This work was performed by Arizona State University as part of a subcontract from the National Renewable Energy Laboratory (NREL). Funding was provided under Agreement 38263 by the U.S. Department of Energy (DOE) Office of Energy Efficiency and Renewable Energy (EERE) Solar Energy Technologies Office (SETO). This work was authored in part by the National Renewable Energy Laboratory, operated by Alliance for Sustainable Energy, LLC, for the U.S. Department of Energy under Contract No. DE-AC36-08GO28308. The views

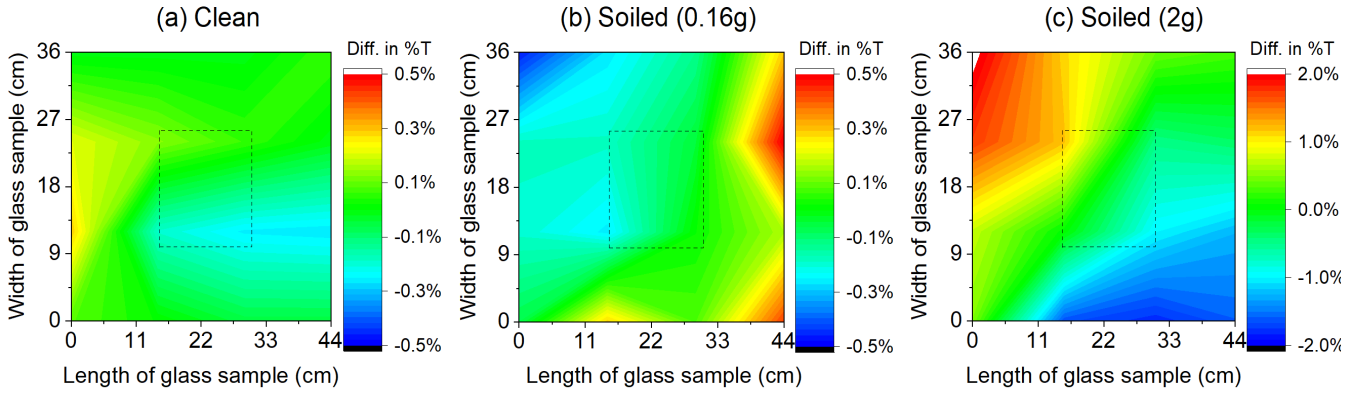

Fig. 11. %T change between %T measured at each spot and average %T across the entire area of the 44 cm x 36 cm glass sample: (a) Clean condition, (b) 0.16 g soiled condition, and (c) 2 g soiled condition. The 15.6 cm x 15.6 cm boxed area in the center of the glass represents the equivalent area of a single solar cell.

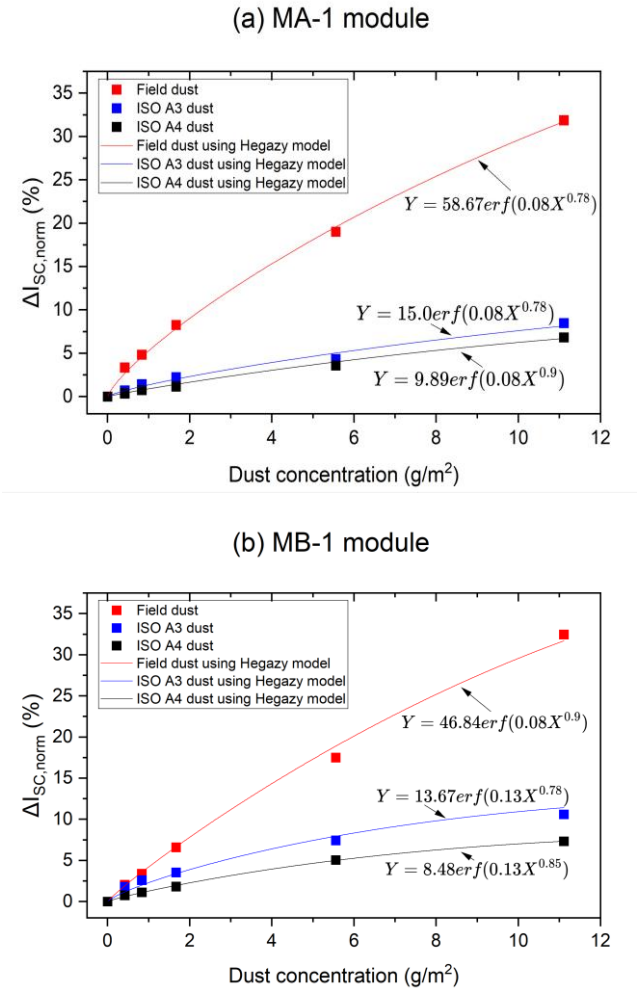

Fig. 12. Empirical fits in $\Delta I_{SC,norm}$ versus dust concentration using Hegazy model for (a) MA-1 module and (b) MB-1 module.

REFERENCES

[1] IEA-PVPS, "Soiling Losses – Impact on the Performance of Photovoltaic Power Plants," IEA PVPS Task 13 - Performance, Operation and Reliability of Photovoltaic Systems Report IEA-PVPS T13-21:2022, Dec. 2022. [Online]. Available: https://iea-pvps.org/wp-content/uploads/2023/01/IEA-PVPS-T13-21-2022-REPORT-Soiling-Losses-PV-Plants.pdf

[2] K. Ilse *et al.*, "Techno-Economic Assessment of Soiling Losses and Mitigation Strategies for Solar Power Generation," *Joule*, vol. 3, no. 10, pp. 2303–2321, Oct. 2019, doi: 10.1016/j.joule.2019.08.019.

[3] J. G. Bessa, L. Micheli, F. Almonacid, and E. F. Fernández, "Monitoring photovoltaic soiling: assessment, challenges, and perspectives of current and potential strategies," *iScience*, vol. 24, no. 3, p. 102165, Mar. 2021, doi: 10.1016/j.isci.2021.102165.

[4] T. M. A. Alnasser, A. M. J. Mahdy, K. I. Abass, M. T. Chaichan, and H. A. Kazem, "Impact of dust ingredient on photovoltaic performance: An experimental study," *Sol. Energy*, vol. 195, pp. 651–659, Jan. 2020, doi: 10.1016/j.solener.2019.12.008.

[5] K. S. AlZahrani, "Experimental investigation of soiling impact on PV module performance in Yanbu Al Sinaiyah, Saudi Arabia," *Renew. Energy*, vol. 216, p. 119117, Nov. 2023, doi: 10.1016/j.renene.2023.119117.

[6] S. S. Hosseini Dehshiri and B. Firoozabadi, "Dust cycle, soiling effect and optimum cleaning schedule for PV modules in Iran: A long-term multi-criteria analysis," *Energy Convers. Manag.*, vol. 286, p. 117084, June 2023, doi: 10.1016/j.enconman.2023.117084.

[7] M. Gostein, J. R. Caron, and B. Littmann, "Measuring soiling losses at utility-scale PV power plants," in *2014 IEEE 40th Photovoltaic Specialist Conference (PVSC)*, Denver, CO, USA: IEEE, June 2014, pp. 0885–0890. doi: 10.1109/PVSC.2014.6925056.

[8] J. Lopez-Garcia, A. Pozza, and T. Sample, "Long-term soiling of silicon PV modules in a moderate subtropical climate," *Sol. Energy*, vol. 130, pp. 174–183, June 2016, doi: 10.1016/j.solener.2016.02.025.

[9] Y. N. Chanchangi, A. Ghosh, S. Sundaram, and T. K. Mallick, "An analytical indoor experimental study on the effect of soiling on PV, focusing on dust properties and PV surface material," *Sol. Energy*, vol. 203, pp. 46–68, June 2020, doi: 10.1016/j.solener.2020.03.089.

[10] P. D. Burton and B. H. King, "Artificial soiling of photovoltaic module surfaces using traceable soil components," in *2013 IEEE 39th Photovoltaic Specialists Conference (PVSC)*, June 2013, pp. 1542–1545. doi: 10.1109/PVSC.2013.6744438.

[11] T. Hirayama *et al.*, "Soiling by volcanic ash fall on photovoltaic modules and effects of hydrophilic coating on module cover glass," *Jpn. J. Appl. Phys.*, vol. 57, no. 8S3, p. 08RG06, Aug. 2018, doi: 10.7567/JJAP.57.08RG06.

[12] L. Fernandes, S. Bhaduri, A. Alath, N. S. Shiradkar, and A. Kottantharayil, "Artificial dust deposition chamber for investigation of soiling loss in photovoltaic modules," in *2019 IEEE 46th Photovoltaic Specialists Conference (PVSC)*, June 2019, pp. 2875–2878. doi: 10.1109/PVSC40753.2019.8981343.

[13] J. J. John, S. Warade, G. Tamizhmani, and A. Kottantharayil, "Study of Soiling Loss on Photovoltaic Modules With Artificially Deposited Dust of Different Gravimetric Densities and Compositions Collected From Different Locations in India," *IEEE J. Photovolt.*, vol. 6, no. 1, pp. 236–243, Jan. 2016, doi: 10.1109/JPHOTOV.2015.2495208.

[14] M.-Á. Muñoz-García, T. Fouris, and E. Pilat, "Analysis of the soiling effect under different conditions on different photovoltaic glasses and cells using an indoor soiling chamber," *Renew. Energy*, vol. 163, pp. 1560–1568, Jan. 2021, doi: 10.1016/j.renene.2020.10.027.

[15] T. Curtis, V. Sreenivash, L. Simpson, and G. TamizhMani, "Effectiveness of Rain Cleaning on Artificially Soiled PV Modules With and Without Anti-soiling Coatings," in *2019 IEEE 46th Photovoltaic Specialists Conference (PVSC)*, June 2019, pp. 2869–2874. doi: 10.1109/PVSC40753.2019.8980742.

[16] M. C. Peel, B. L. Finlayson, and T. A. McMahon, "Updated world map of the Köppen-Geiger climate classification," *Hydrol. Earth Syst. Sci.*, vol. 11, no. 5, pp. 1633–1644, Oct. 2007, doi: 10.5194/hess-11-1633-2007.

[17] F. A. Mejia and J. Kleissl, "Soiling losses for solar photovoltaic systems in California," *Sol. Energy*, vol. 95, pp. 357–363, Sept. 2013, doi: 10.1016/j.solener.2013.06.028.

[18] A. Kimber, L. Mitchell, S. Nogradi, and H. Wenger, "The Effect of Soiling on Large Grid-Connected Photovoltaic Systems in California and the Southwest Region of the United States," in *2006 IEEE 4th World Conference on Photovoltaic Energy Conference*, May 2006, pp. 2391–2395. doi: 10.1109/WCPEC.2006.279690.

[19] S. Warade and A. Kottantharayil, "Analysis of Soiling Losses for Different Cleaning Cycles," in *2018 IEEE 7th World Conference on Photovoltaic Energy Conversion (WCPEC) (A Joint Conference of 45th IEEE PVSC, 28th PVSEC & 34th EU PVSEC)*, June 2018, pp. 3644–3647. doi: 10.1109/PVSC.2018.8547867.

[20] S. Bhaduri and A. Kottantharayil, "Mitigation of Soiling by Vertical Mounting of Bifacial Modules," *IEEE J. Photovolt.*, vol. 9, no. 1, pp. 240–244, Jan. 2019, doi: 10.1109/JPHOTOV.2018.2872555.

[21] A. Ullah, A. Amin, T. Haider, M. Saleem, and N. Z. Butt, "Investigation of soiling effects, dust chemistry and optimum cleaning schedule for PV modules in Lahore, Pakistan," *Renew. Energy*, vol. 150, pp. 456–468, May 2020, doi: 10.1016/j.renene.2019.12.090.

[22] R. R. Cordero *et al.*, "Effects of soiling on photovoltaic (PV) modules in the Atacama Desert," *Sci. Rep.*, vol. 8, no. 1, p. 13943, Sept. 2018, doi: 10.1038/s41598-018-32291-8.

[23] A. M. Al-Sabounchi, S. A. Yalyali, and H. A. Al-Thani, "Design and performance evaluation of a photovoltaic grid-connected system in hot weather conditions," *Renew. Energy*, vol. 53, pp. 71–78, May 2013, doi: 10.1016/j.renene.2012.10.039.

[24] N. Hussain *et al.*, "Designing of homemade soiling station to explore soiling loss effects on PV modules," *Sol. Energy*, vol. 225, pp. 624–633, Sept. 2021, doi: 10.1016/j.solener.2021.07.036.

[25] A. Heimsath *et al.*, "Specular reflectance of soiled glass mirrors – Study on the impact of incidence angles," presented at the SOLARPACES 2015: International Conference on Concentrating Solar Power and Chemical Energy Systems, Cape Town, South Africa, 2016, p. 130009. doi: 10.1063/1.4949219.

[26] P. Ravi *et al.*, "Indoor Soil Deposition Chamber: Evaluating Effectiveness of Antisoiling Coatings," *IEEE J. Photovolt.*, vol. 9, no. 1, pp. 227–232, Jan. 2019, doi: 10.1109/JPHOTOV.2018.2877021.

[27] K. Ilse, M. Z. Khan, N. Voicu, V. Naumann, C. Hagendorf, and J. Bagdahn, "Advanced performance testing of anti-soiling coatings – Part I: Sequential laboratory test methodology covering the physics of natural soiling processes," *Sol. Energy Mater. Sol. Cells*, vol. 202, p. 110048, Nov. 2019, doi: 10.1016/j.solmat.2019.110048.

[28] M. Z. Khan *et al.*, "Correlation between laboratory and outdoor soiling experiments with anti-soiling coatings," *Sol. Energy Mater. Sol. Cells*, vol. 269, p. 112751, June 2024, doi: 10.1016/j.solmat.2024.112751.

[29] Z. Hammond, T. Curtis, L. Simpson, and G. TamizhMani, "Design Advancement of an Indoor Soil Deposition Chamber: A Road to Standardization," in *2019 IEEE 46th Photovoltaic Specialists Conference (PVSC)*, June 2019, pp. 3263–3268. doi: 10.1109/PVSC40753.2019.8981244.

[30] M. Gostein, B. Littmann, J. R. Caron, and L. Dunn, "Comparing PV power plant soiling measurements extracted from PV module irradiance and power measurements," in *2013 IEEE 39th Photovoltaic Specialists Conference (PVSC)*, June 2013, pp. 3004–3009. doi: 10.1109/PVSC.2013.6745094.

[31] IEC 61724-1:2021, *Photovoltaic system performance - Part 1: Monitoring*, 2021. [Online]. Available: https://webstore.iec.ch/en/publication/65561

[32] US EPA, "Download Daily Data." [Online]. Available: https://www.epa.gov/outdoor-air-quality-data/download-daily-data

[33] R. J. Isaifan, D. Johnson, L. Ackermann, B. Figgis, and M. Ayoub, "Evaluation of the adhesion forces between dust particles and photovoltaic module surfaces," *Sol. Energy Mater. Sol. Cells*, vol. 191, no. November 2018, pp. 413–421, 2019, doi: 10.1016/j.solmat.2018.11.031.

[34] S. Sengupta, S. Sengupta, and H. Saha, "Comprehensive Modeling of Dust Accumulation on PV Modules through Dry Deposition Processes," *IEEE J. Photovolt.*, vol. 10, no. 4, pp. 1148–1157, 2020, doi: 10.1109/JPHOTOV.2020.2992352.

[35] M. Deceglie, "Photovoltaic Module Soiling Map," National Renewable Energy Laboratory (NREL). [Online]. Available: https://www.nrel.gov/pv/soiling.html#pvsoiling-activelocation-wrapper

[36] M. G. Lawrence, "The Relationship between Relative Humidity and the Dewpoint Temperature in Moist Air: A Simple Conversion and Applications," *Bull. Am. Meteorol. Soc.*, vol. 86, no. 2, pp. 225–234, Feb. 2005, doi: 10.1175/BAMS-86-2-225.

[37] S. Ibrahim *et al.*, "Water Interaction with Mineral Dust Aerosol: Particle Size and Hygroscopic Properties of Dust," *ACS Earth Space Chem.*, vol. 2, no. 4, pp. 376–

386, Apr. 2018, doi: 10.1021/acsearthspacechem.7b00152.

[38] C. E. Commission, "PV Module List - Full Data | California Energy Commission." [Online]. Available: https://www.energy.ca.gov/media/2367

[39] G. P. Smestad *et al.*, "Modelling photovoltaic soiling losses through optical characterization," *Sci. Rep.*, vol. 10, no. 1, p. 58, Jan. 2020, doi: 10.1038/s41598-019-56868-z.

[40] ISO 12103-1:2024, *Road vehicles — Test contaminants for filter evaluation — Part 1: Arizona test dust*. [Online]. Available: https://www.iso.org/standard/85949.html

[41] T. Hashimoto, T. Yamada, and T. Yoko, "Third-order nonlinear optical properties of sol–gel derived α-Fe2O3, γ-Fe2O3, and Fe3O4 thin films," *J. Appl. Phys.*, vol. 80, no. 6, pp. 3184–3190, Sept. 1996, doi: 10.1063/1.363258.

[42] C. Linke *et al.*, "Optical properties and mineralogical composition of different Saharan mineral dust samples: a laboratory study," *Atmospheric Chem. Phys.*, vol. 6, no. 11, pp. 3315–3323, Aug. 2006, doi: 10.5194/acp-6-3315-2006.

[43] Q. Fang, H. Hong, L. Zhao, S. Kukolich, K. Yin, and C. Wang, "Visible and Near-Infrared Reflectance Spectroscopy for Investigating Soil Mineralogy: A Review," *J. Spectrosc.*, vol. 2018, no. 1, p. 3168974, 2018, doi: 10.1155/2018/3168974.

[44] R. M. Cornell and U. Schwertmann, *The Iron Oxides: Structure, Properties, Reactions, Occurrences and Uses*. Newark, Germany: John Wiley & Sons, Incorporated, 2003. [Online]. Available: https://scholar.google.com/scholar?hl=en&as_sdt=0%2C3&q=The+Iron+Oxides%3A+Structure%2C+Properties%2C+Reactions%2C+Occurrences+and+Uses.&btnG=

[45] D. B. Curtis *et al.*, "A laboratory investigation of light scattering from representative components of mineral dust aerosol at a wavelength of 550 nm," *J. Geophys. Res. Atmospheres*, vol. 113, no. D8, 2008, doi: 10.1029/2007JD009387.

[46] D. Goossens and E. V. Kerschaever, "Aeolian dust deposition on photovoltaic solar cells: The effects of wind velocity and airborne dust concentration on cell performance," *Sol. Energy*, vol. 66, no. 4, pp. 277–289, 1999, doi: 10.1016/S0038-092X(99)00028-6.

[47] R. A. Viscarra Rossel, B. Minasny, P. Roudier, and A. B. McBratney, "Colour space models for soil science," *Geoderma*, vol. 133, no. 3, pp. 320–337, Aug. 2006, doi: 10.1016/j.geoderma.2005.07.017.

[48] C. Hu, H. Guo, H. Mei, and J. Zhu, "Prediction of iron content in soil based on microspectrophotometry analysis," *Forensic Sci. Int.*, vol. 318, p. 110600, Jan. 2021, doi: 10.1016/j.forsciint.2020.110600.

[49] J. Madeira, A. Bedidi, B. Cervelle, M. Pouget, and N. Flay, "Visible spectrometric indices of hematite (Hm) and goethite (Gt) content in lateritic soils: The application of a Thematic Mapper (TM) image for soil-mapping in Brasilia, Brazil," *Int. J. Remote Sens.*, vol. 18, no. 13, pp. 2835–2852, Sept. 1997, doi: 10.1080/014311697217369.

[50] F. Corsini *et al.*, "Highly emissive fluorescent silica-based core/shell nanoparticles for efficient and stable luminescent solar concentrators," *Nano Energy*, vol. 80, p. 105551, Feb. 2021, doi: 10.1016/j.nanoen.2020.105551.

[51] S. Toth *et al.*, "Soiling and cleaning: Initial observations from 5-year photovoltaic glass coating durability study," *Sol. Energy Mater. Sol. Cells*, vol. 185, pp. 375–384, Oct. 2018, doi: 10.1016/j.solmat.2018.05.039.

[52] H. F. Varga and M. R. Wiesner, "Effect of Dust Composition on the Reversibility of Photovoltaic Panel Soiling," *Environ. Sci. Technol.*, vol. 55, no. 3, pp. 1984–1991, Feb. 2021, doi: 10.1021/acs.est.0c06196.

[53] M. Nocita, A. Stevens, G. Toth, P. Panagos, B. van Wesemael, and L. Montanarella, "Prediction of soil organic carbon content by diffuse reflectance spectroscopy using a local partial least square regression approach," *Soil Biol. Biochem.*, vol. 68, pp. 337–347, Jan. 2014, doi: 10.1016/j.soilbio.2013.10.022.

[54] S. C. Alfaro, S. Lafon, J. L. Rajot, P. Formenti, A. Gaudichet, and M. Maillé, "Iron oxides and light absorption by pure desert dust: An experimental study," *J. Geophys. Res. Atmospheres*, vol. 109, no. D8, Apr. 2004, doi: 10.1029/2003JD004374.

[55] A. Ciani, K.-U. Goss, and R. P. Schwarzenbach, "Light penetration in soil and particulate minerals," *Eur. J. Soil Sci.*, vol. 56, no. 5, pp. 561–574, 2005, doi: 10.1111/j.1365-2389.2005.00688.x.

[56] T. H. Waiser, C. L. S. Morgan, D. J. Brown, and C. T. Hallmark, "In Situ Characterization of Soil Clay Content with Visible Near-Infrared Diffuse Reflectance Spectroscopy," *Soil Sci. Soc. Am. J.*, vol. 71, no. 2, pp. 389–396, 2007, doi: 10.2136/sssaj2006.0211.

[57] R. N. Clark and T. L. Roush, "Reflectance spectroscopy: Quantitative analysis techniques for remote sensing applications," *J. Geophys. Res. Solid Earth*, vol. 89, no. B7, pp. 6329–6340, 1984, doi: 10.1029/JB089iB07p06329.

[58] H. Buddenbaum and M. Steffens, "The Effects of Spectral Pretreatments on Chemometric Analyses of Soil Profiles Using Laboratory Imaging Spectroscopy," *Appl. Environ. Soil Sci.*, vol. 2012, no. 1, p. 274903, 2012, doi: 10.1155/2012/274903.

[59] M. Ladoni, H. A. Bahrami, S. K. Alavipanah, and A. A. Norouzi, "Estimating soil organic carbon from soil reflectance: a review," *Precis. Agric.*, vol. 11, no. 1, pp. 82–99, Feb. 2010, doi: 10.1007/s11119-009-9123-3.

[60] N. Richter, T. Jarmer, S. Chabrillat, C. Oyonarte, P. Hostert, and H. Kaufmann, "Free Iron Oxide Determination in Mediterranean Soils using Diffuse Reflectance Spectroscopy," *Soil Sci. Soc. Am. J.*, vol. 73, no. 1, pp. 72–81, 2009, doi: 10.2136/sssaj2008.0025.

[61] A. C. Scheinost, A. Chavernas, V. Barrón, and J. Torrent, "Use and Limitations of Second-Derivative Diffuse Reflectance Spectroscopy in the Visible to Near-Infrared Range to Identify and Quantify Fe Oxide

Minerals in Soils," *Clays Clay Miner.*, vol. 46, no. 5, pp. 528–536, Oct. 1998, doi: 10.1346/CCMN.1998.0460506.

[62] E. Ben-Dor, Y. Inbar, and Y. Chen, "The reflectance spectra of organic matter in the visible near-infrared and short wave infrared region (400–2500 nm) during a controlled decomposition process," *Remote Sens. Environ.*, vol. 61, no. 1, pp. 1–15, July 1997, doi: 10.1016/S0034-4257(96)00120-4.

[63] S. Miranda, A. Vilanova, T. Lopes, and A. Mendes, "TiO 2 -coated window for facilitated gas evolution in PEC solar water splitting," *RSC Adv.*, vol. 7, no. 47, pp. 29665–29671, 2017, doi: 10.1039/C7RA01923H.

[64] M. A. M. L. D. Jesus, G. Timò, C. Agustín-Sáenz, I. Braceras, M. Cornelli, and A. D. M. Ferreira, "Anti-soiling coatings for solar cell cover glass: Climate and surface properties influence," *Sol. Energy Mater. Sol. Cells*, vol. 185, pp. 517–523, Oct. 2018, doi: 10.1016/j.solmat.2018.05.036.

[65] S. F. Bukhari, F. Lisco, T. B. Moghim, A. Taylor, and J. M. Walls, "Development of a Hydrophobic, Anti-soiling coating for PV Module Cover Glass," in *2019 IEEE 46th Photovoltaic Specialists Conference (PVSC)*, June 2019, pp. 2849–2853. doi: 10.1109/PVSC40753.2019.8981377.

[66] J. Wohlgemuth and S. Kurtz, "Photovoltaic Module Qualification Plus Testing," in *2014 IEEE 40th Photovoltaic Specialist Conference, PVSC 2014*, 2014, pp. 3589–3594. doi: 10.1109/PVSC.2014.6924883.

[67] IEC TS 62788-7-2:2017, *Measurement procedures for materials used in photovoltaic modules - Part 7-2: Environmental exposures - Accelerated weathering tests of polymeric materials*. [Online]. Available: https://webstore.iec.ch/en/publication/33675

[68] IEC 61215-1:2021, *Terrestrial photovoltaic (PV) modules - Design qualification and type approval - Part 1: Test requirements*, Feb. 23, 2021. [Online]. Available: https://webstore.iec.ch/en/publication/61345

[69] VDI 3956 Blatt 1, *Evaluation of the soiling properties of surfaces - Test method for the dust soiling behaviour of solar energy systems*, Sept. 2020. [Online]. Available: https://www.vdi.de/en/home/vdi-standards/details/vdi-3956-blatt-1-evaluation-of-the-soiling-properties-of-surfaces-test-method-for-the-dust-soiling-behaviour-of-solar-energy-systems

[70] A. A. Hegazy, "Effect of dust accumulation on solar transmittance through glass covers of plate-type collectors," *Renew. Energy*, vol. 22, no. 4, pp. 525–540, Apr. 2001, doi: 10.1016/S0960-1481(00)00093-8.

[71] M. Mani and R. Pillai, "Impact of dust on solar photovoltaic (PV) performance: Research status, challenges and recommendations," *Renew. Sustain. Energy Rev.*, vol. 14, no. 9, pp. 3124–3131, Dec. 2010, doi: 10.1016/j.rser.2010.07.065.